

Fluorescence Microscopy And Histopathology Image Based Cancer Classification Using Graph Convolutional Network With Channel Splitting

Asish Bera^{a,*}, Debotosh Bhattacharjee^{b,c} and Ondrej Krejcar^{c,d,e}

^aDepartment of Computer Science and Information Systems BITS Pilani Pilani Campus Rajasthan 333031 India

^bDepartment of Computer Science and Engineering Jadavpur University Kolkata West Bengal 700032 India

^cCenter for Basic and Applied Science Faculty of Informatics and Management University of Hradec Kralove Rokitanskeho 62 500 03 Czech Republic

^dSkoda Auto University Na Karmeli 1457 293 01 Mlada Boleslav Czech Republic

^eMalaysia Japan International Institute of Technology (MJIIT) Universiti Teknologi Malaysia Kuala Lumpur Malaysia

ARTICLE INFO

Keywords:

Histopathology
Channel Splitting
Cancer Cell Classification
Fluorescence Microscopy
Graph Convolutional Network.

ABSTRACT

Since the proliferation of deep learning, several convolutional neural networks (CNNs) are developed to attain significant breakthroughs for automated cancer classification using histopathology and fluorescence microscopy images. This work enhances the classification performances of human breast and lung-colon cancers further by exploring a two-layer graph convolutional network (GCN) upon a proposed lightweight deep convolutional backbone or existing pre-trained CNN. The first graph convolution layer considers local regions as the graph nodes with channel information as node features. The second layer is rendered by pooling and splitting the output feature map of former layer into a low dimensional feature vector that serves as node features. The proposed method, named Channel-Splitting Graph Convolutional Network (CS-GCN), enhances holistic feature representation of spatial structural information. The significance of region-aware distinctness is explored for building a correlation among neighboring regions through node-level mixed feature propagation of a graph. The experiments are carried out on three public datasets, representing the breast cancer (actin-labeled fluorescence microscopy image dataset (FMID), and BreakHis dataset with four magnifications), and lung-colon cancer (LC25000 dataset). The top-1 classification accuracies attained by CS-GCN using ResNet-50 backbone on the FMID: 99.30%, BreakHis 40x: 98.0%, BreakHis 100x: 97.81%, BreakHis 200x: 97.33%, BreakHis 400x: 96.85%, and LC25000: 100.0%. The performances are improved on these datasets, while built upon a proposed convolutional stem as well as pre-trained ResNet-50 and DenseNet-201 backbones, implying the effectiveness of the proposed CS-GCN. The source codes are available at: <https://github.com/asish-bera/CS-GCN>.

1. Introduction

Advances in deep neural networks have broadened the pathways of profound signal processing applications in healthcare domain including cancer diagnosis, biomedical analysis, and many more AlQuraishi and Sorger (2021), Razmjoooy, Ramezani and Ghadimi (2017), Jabeen, Khan, Damaševičius, Alsenan, Baili, Zhang and Verma (2024a), Li, Daho, Conze, Zeghlache, Le Boit  , Tadayoni, Cochener, Lamard and Quellec (2024c). Breast and lung cancers are two most widely diagnosed cancer types across the world. Diagnosis of cancer at early-stages leveraging machine learning (ML) increase survival rates Pan, Hua, Tong, Li, Luo, Yang and Ding (2025), Abbas, Le Vuong, Kim, Song and Kwak (2023), Talib, Amin, Sharif and Raza (2024). The histopathology and fluorescence microscopy images represent crucial phenotypic information, which is indispensable for accurate pathological diagnosis of breast cancer. The diagnosis by human experts requires domain knowledge Oei, Hou, Liu, Zhong, Zhang, An, Xu and Yang (2019). Also, proper treatment is a sensitive and labor-intensive task, and

expensive for common people. The cost of cancer prognosis can be reduced using computer-aided diagnosis (CAD) tools T  ga  r,   zkurt, Ergen and C  mert (2020).

The rapid increase of biomedical and pathological images of breast and lung cancers have guided deep learning methods to attain significant breakthroughs in medical imaging Li, Mei, Li, Yu and Liu (2024a), Abdulaal, Valizadeh, Amirani and Shah (2024), Cai, Li, Razmjoooy and Ghadimi (2021), Fu, Chen, Wang and Huang (2025), Jabeen, Khan, Hameed, Alqahtani, Alouane and Masood (2024b). Beyond binary classification, sub-categorization of multi-class breast and lung cancer is a vital image recognition challenge due to subtle variations in cell structures, illumination, and external environment. In addition, normal and benign cells exhibit various mechanical properties. Also, cancer cells have irregular and abnormal growth. Thus, structural information and organization of cells is pivotal for determining the malignant cells and can be utilized as a diagnostic marker, which is beyond human inspection. Moreover, cell classification relying on the subcellular features and actin filaments (e.g., human breast epithelial cell lines, Fig. 4) is a complex image recognition problem that has not been explored widely in prior works Oei et al. (2019). Thus, cancer cell classification with high precision is considered to be a challenging job.

*Corresponding author

 asish.bera@pilani.bits-pilani.ac.in (A. Bera); debotosh.bhattacharjee@jadavpuruniversity.in (D. Bhattacharjee); ondrej.krejcar@uhk.cz (O. Krejcar)

Convolutional neural networks (CNNs) and related deep learning (DL) techniques provide fast and accurate cancer classification results, leading to early detection of various types of cancers e.g., breast, skin, lung, etc. Zhang, Zhang, Gao, Bai, Li and Ghadimi (2024a), Razmjoojy, Sheykhamad and Ghadimi (2018), Xu, Sheykhamad, Ghadimi and Razmjoojy (2020), Han, Zhao, Yin, Hu and Ghadimi (2024), Bera, Bhattacharjee and Nasipuri (2022a). Several works have addressed cancer classification using histopathology images, and especially, actin labeled fluorescence microscopy images. However, most of the available methods on breast cancers studied binary classification (i.e., malignant or benign) and achieved high performances, e.g., BreastNet Toğaçar et al. (2020), CSF transformer Huang, Yu, Huang and Cheng (2023), transfer learning methods Almaslukh (2024), Maurya, Pandey, Dutta and Karnati (2024), etc. A few ML/DL works experimented with multi-class categorization of breast cancers, providing more accurate insights for better diagnosis and treatment e.g., BHCNet Jiang, Chen, Zhang and Xiao (2019). Some studies explored transfer learning and fusion methods with pre-trained CNNs to tackle this problem Jabeen, Khan, Alhaisoni, Tariq, Zhang, Hamza, Mickus and Damaševičius (2022).

Graph convolutional network (GCN), a popular variant of graph neural network (GNN), can be integrated with traditional CNN to build a graph structure comprising with nodes and edges Kipf and Welling (2017). Other variations of GNN include graph recurrent neural network, graph attention network, etc. GCN is suitable for solving classification of different types of human and plant diseases, human actions, etc. Berenguer, Kvasnytsia, Bossa, Mukherjee, Deligiannis and Sahli (2024), Bera, Bhattacharjee and Krejcar (2024a), Chen, Zhou, Ke, Huang, Xiong, Huang, Ma, Ning, Wu and Wu (2023), Liu and Ghadimi (2024), D’Souza, Wang, Giovannini, Foncubierta-Rodriguez, Beck, Boyko and Syeda-Mahmood (2024). Though diverse GCNs proved their efficacy in classifying histopathology, mammogram, MRI, and other categories of images, yet, more attention should be given for addressing challenges pertinent to medical image/signal processing. Existing works show pathways of GCNs in capturing relevant spatial descriptors for improving CAD performances Ding, Gao, Wang, Lu and Shi (2023), multi-level fusion of graphs for capturing topological relationships Peng, Peng, Zhou, Han, Xu, Lu and Lv (2024), etc. However, channel-wise feature calibration utilizing GCN that facilitates effective feature selection is not studied in existing works. This work develops a multi-layer GCN for learning region-aware semantics and enhancing feature summarization by channel-wise feature mixing. The GCN enables to recognize sub-classes of a variety of histopathology image datasets with enhanced performances.

Here, the importance of local contextual regions is propagated through the nodes of a spatial graph. A new feature aggregation scheme is developed by mixing node-level features, and then splitting them by down-sampling into a low dimension for selecting discriminative features through a graph convolution layer. The proposed method

offers a lower computational cost by developing a base convolutional stem. The proposed method, named channel-splitting graph convolutional network (CS-GCN), demonstrates multi-classification of breast and lung-colon cancer sub-types. The contributions of this work are:

- A graph-based feature learning method using a two-layer GCN is integrated upon a CNN backbone for the classification of breast and lung-colon cancers.
- The proposed method develops a low resource-intensive framework (i.e., lightweight deep learning model) by splitting and mixing node features of a spatial graph for precise feature representation.
- Performance improvement over existing methods on three public datasets, representing fluorescence microscopy images of breast, and histopathological images of breast and lung-colon cancers. The experimental evaluations evince superiority of proposed work.

The rest of this article is organized as follows: Section 2 summarizes related works. Section 3 describes the proposed methodology. The experimental results are showcased in Section 4, followed by the conclusion in Section 5.

2. Related Works

Various cancer classification methods using artificial intelligence (AI) and machine learning (ML) techniques are summarized by Ramirez-Bautista, Chaparro-Cárdenas, Esmer and Huerta-Ruelas (2024). Handcrafted feature descriptors (e.g., Hu moment, Haralick textures, etc.) and CNNs were employed for breast cancer multi-classification using histopathology images of the BreakHis dataset Joseph, Abdullahi, Junaidu, Ibrahim and Chiroma (2022), Xiao, Li, Yan, Gao and Wang (2024).

2.1. Breast Cancer Classification Methods

A self-distilled supervised contrastive learning method was presented for automated diagnosis of breast cancers with limited histopathology training samples Gong, Wang, Wang, Ge, Yu and Shi (2022). The inception recurrent residual CNN was developed for histopathology image classification on the same dataset Alom, Yakopcic, Nasrin, Taha and Asari (2019). Pre-trained CNNs particularly the VGG-19, MobileNet, and DenseNet were ensembled for classifying breast histology images Kassani, Kassani, Wesolowski, Schneider and Deters (2019). A self-supervised federated learning framework enhanced the diagnostic accuracy and generalization ability Zhang, Li, Han, Ding, Li, Wang, Ying and Shi (2024b). An automated method of molecular subtyping of breast cancer was studied Niyas, Bygari, Naik, Viswanath, Ugwekar, Mathew, Kavya, Kini and Rajan (2023). Multi-stage transfer learning approach relying on domain adaptation tested for classifying histopathology images Mudeng, Farid, Ayana and Choe (2023). These works illustrate diverse learning strategies developed for cancer classification using CNNs and fusion strategies.

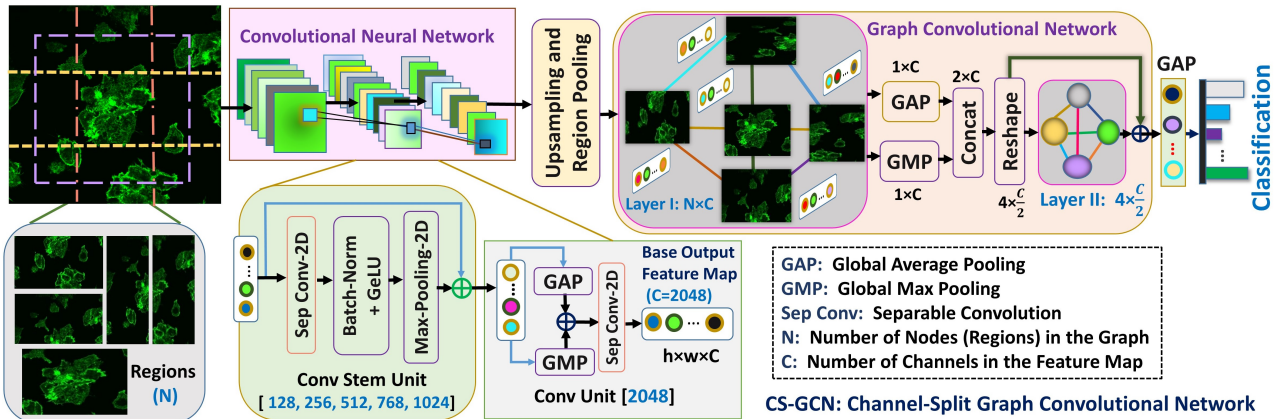


Figure 1: Proposed Channel-Splitting Graph Convolutional Network (CS-GCN) is built upon a lightweight convolutional stem with pooled regions for constructing a region-aware spatial graph. The CS-GCN is developed for breast and lung cancer multi-class categorization using fluorescence and histopathology microscopy images.

Attention methods are developed for progressing state-of-the-art further in medical diagnosis, human action, object classification and many other tasks Bera, Krejcar and Bhattacharjee (2024b), Bera, Nasipuri, Krejcar and Bhattacharjee (2023). A multi-level fully convolutional attention network, called FCCS-Net, tested for breast cancer classification using transfer learning Maurya et al. (2024). A multi-scale dual-adaptive attention network relying on DenseNet was presented for breast cancer pathological image classification Li, Long, Zhan and Wu (2024b). A holistic attention network extended the bag-of-words model using Transformer for classifying breast biopsy images Mehta, Lu, Wu, Weaver, Hajishirzi, Elmore and Shapiro (2022). MbsCANet Cao, Pan, Ren, Lu and Zhang (2024) represented a multi-branch spectral channel attention network that combined the lowest frequency features with selected high frequency information from two-dimensional discrete cosine transform. DinNet exploited an attention mechanism underlying an improved DenseNet model Guo, Lin, Ji, Han, Liao, Shen, Feng and Tang (2024). These attention methods emphasize relevant features for discriminating various types of cancer images.

A study combined convolutional networks and vision transformers and tested on five histopathology datasets in addition to assessing the robustness using a generative adversarial network (GAN) Springenberg, Frommholz, Wenzel, Weicken, Ma and Strodthoff (2023). An ensemble of Swin transformers (i.e., tiny, small, base, and large) was developed for classifying the BreakHis samples Tummala, Kim and Kadry (2022). A dual-branch dual-task adaptive cross-weight feature fusion network integrated heterogeneous feature representations from CNN and transformers for cancer classification Bui, Song, Kim and Kwak (2024). A recent work has applied a Swin transformer for feature extraction to develop a two-fold feature fusion method Hao, Jia, Liu, Wang, Liu, Ji and Ganchev (2024). Notably, transformer models also evince their suitability for cancer classification.

2.1.1. GCN Based Approaches

Graph based message passing techniques through GCNs are used for medical diagnosis, generic object classification,

and others Bera, Wharton, Liu, Bessis and Behera (2022b). A multi-cell type and multi-level graph aggregation network was developed for cancer grading Abbas et al. (2023). A MLP-mixer-based multi-path feature fusion combined multi-level graph features with fractal structures from multiple paths for classifying histopathology images Ding et al. (2023). An automated breast cancer diagnosis method optimized with higher-order attribute enhancing heterogeneous GCN was presented using distributed nonlinear polynomial graph filter for quality enhancement and noise removal from mammogram images Kulandaivelu, Taluja, Gawas and Nath (2024). The PND-Net applied a two-layer GCN for classifying the BreakHis 40x and 100x samples Bera et al. (2024a). A label diffusion graph learning method was presented for breast cancer recognition in a semi-supervised framework Zeng and Xu (2023). An embedded fusion mutual learning was developed using an adaptive feature fusion classifier for breast and lung-colon cancer classification Li, Wu, Xu, Li, Zhu, Ye and Zhang (2023a). A cervical cell classification method applied worse-case boosting for learning from under-representative datasets Song, Zou, Choi, Lei and Qin (2024). Multi-modal fusion with a GCN has been studied for clinical analysis D'Souza et al. (2024). Delving into the depth of spatial graph structures, this work develops a GCN with channel interaction for classifying cancer images.

2.1.2. Breast Cancer Fluorescence Microscopy Images

In another direction, CNNs were applied for cell classification based on actin-labeled fluorescence microscopy images, consisting of normal breast epithelial cell line, and two distinct types of breast cancer cell lines Oei et al. (2019). Following similar line of study, transfer learning-based multi-level ensemble technique was developed for classifying cell images captured by a immunofluorescence confocal microscopy and other imaging techniques for generalization Maurya, Pathak and Dutta (2021).

2.2. Methods on Lung-Colon Cancer

A lightweight deep model was developed for mobile-edge computing devices using microscopy images and attained superior performances for lung cancer classification

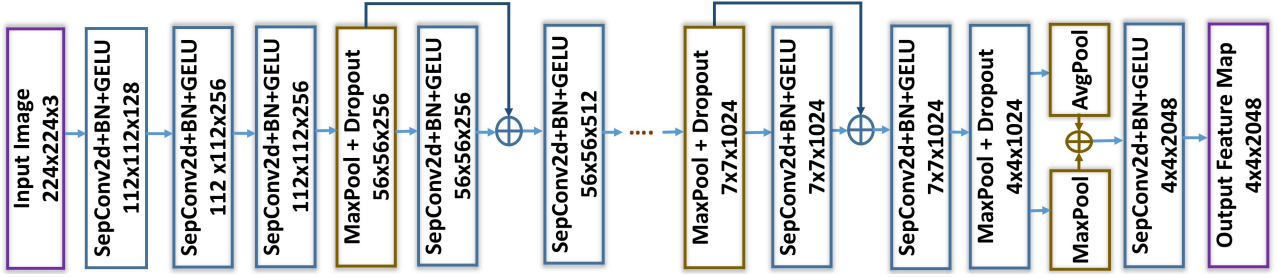


Figure 2: Model architecture of the proposed lightweight convolutional stem (CNN).

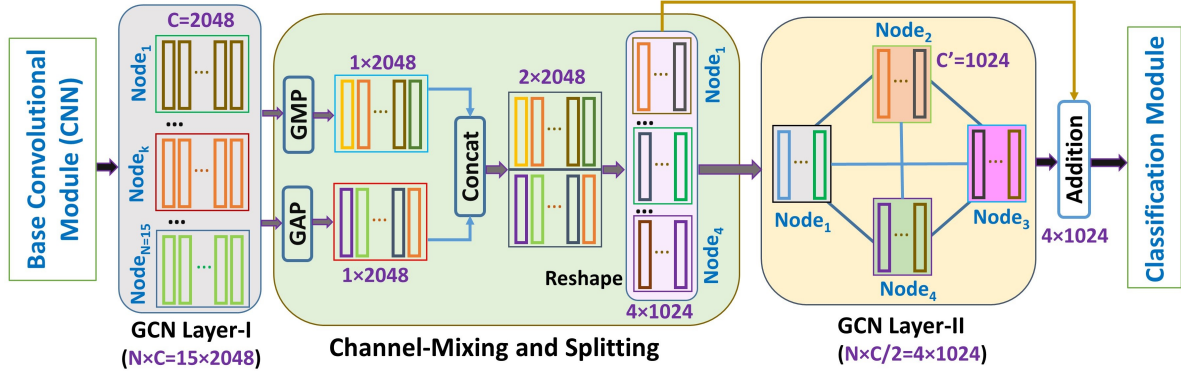


Figure 3: Proposed channel-mixing and splitting technique for GCN-based feature propagation.

Biswas and Barma (2024). An on-cloud decision support system for non-small cell lung cancer histology was developed by Tomassini, Falcionelli, Bruschi, Sbrollini, Marini, Sernani, Morettini, Müller, Dragoni and Burattini (2023). A multi-modal lung-colon cancer classification method using dense networks was described Uddin, Chen, Akter, Ku, Yang and Por (2024). Recently, HookEfficientNet was developed for non-small cell lung cancer recognition Yuan, Kido, Hirata, Ueno, Imai, Chen, Ren, Yang, Chen, Qu et al. (2024).

Inspired with these decent progress, this work generalizes suitability of GCN by developing a convolutional stem attributed with low computational overhead for breast and lung-colon cancer multi-classification using fluorescence microscopy and histopathology images.

3. Proposed Methodology

The proposed method comprises two sub-networks: i) a base convolutional stem that can be alternatively replaced with a standard base CNN e.g., ResNet, DenseNet, etc. (ii) a two-layer GCN with channel-splitting (CS-GCN) to squeeze the feature space for aggregation. The proposed CS-GCN is added upon a base CNN, shown in Fig. 1.

3.1. Base Convolutional Stem (CNN)

An input image, denoted with the class-label $I_l \in \mathbb{R}^{h \times w \times 3}$, is used to extract high-level deep features utilizing a CNN model. Among several CNN backbone families, residual, inception, and others have widely been used in the literature He, Zhang, Ren and Sun (2016). Besides, few works devised different CNN/stems using stacking

multiple convolutional blocks Truong, Philips and Veelaert (2024). A general convolution intrinsically requires more model parameters compared to the depth-wise separable convolution (*SepConv*) due to architectural design Chollet (2017). Also, *SepConv* offers better performances over other CNNs e.g., VGG family. Here, a convolutional stem is built using *SepConv* blocks, akin to a standard CNN backbone. The aim is to develop an efficient deep network for achieving competitive performance with respect to other backbones while trained with random initialization.

In depth-wise separable convolution, spatial convolution is applied to each channel independently, followed by point-wise convolution for transforming and projecting the channels into a new feature map. Clearly, this two-fold factoring technique decouples the feature map following spatial and channel-wise aspects for improving the learning performance. Yet, *SepConv* offers a low-rank factorization for spatial and channel-wise interactions. It is easy to use by replacing traditional convolution as *SepConv* requires lesser parameters Chollet (2017). Now, as the proposed stem is built with only a very less number of layers, aiming for a shallower architecture than existing deeper models, thus, it is lightweight. Details of the CNN/stem are provided below.

$$\mathbf{F}_{ConvBlock[k]}^{(l+1)} = BatchNorm(GELU(SepConv(\mathbf{F}^l)\mathcal{W}^l + b^l)) \quad (1)$$

The building block of proposed stem is *SepConv* with increasing channel size following residual blocks (*ConvBlock[k]*) of sizes $[k] = [128, 256, 512, 768, 1024, 2048]$.

In addition, commonly used downsampling by max-pooling, the Gaussian Error Linear Unit (GELU) activation Hendrycks and Gimpel (2016), dropout, and *BatchNorm* layers are included in the network to improve the learning capacity. The convolutional stem (CNN) is shown block-wise in Fig. 2, and defined in eq. 1. Next, the output feature maps are mixed and aggregated along the channels using global average pooling (GAP) and global max pooling (GMP) layers. This feature-level aggregation is beneficial for selecting discriminatory information by mixing both max and average pooling strategies rather than using any one pooling. Subsequently, the last *SepConv* computes convolutional features with 2048 filters. The base output feature map is denoted as $\mathbf{F} \in \mathbb{R}^{h \times w \times C}$ where h , w , and C imply the height, width, and channels, respectively. The weight is $\mathcal{W}^{(l)}$ and the bias is b^l at l^{th} layer.

As deep layers represent high-level features, spatial references are squeezed into a reduced resolution, which might be enough to define an end-to-end network for solving generic image classification. However, in many complex visual recognition problems, such as the current one for addressing microscopy images, this type of generic CNN backbone having huge model parameters is not always beneficial for capturing discriminatory features from non-uniform cancer cell structures, resulting in underrepresented data. Also, standard pre-trained deep models (e.g., VGG, ResNet, etc.) are trained on generic object categories, which often ignore relevant information for learning structural details from biological cells. Hence, a sophisticated and lightweight backbone network is crucial for solving medical image recognition which is proposed here.

3.2. Region-Aware Feature Computation

Contextual information is crucial for aggregating structural content of image-level descriptions into a holistic feature map. It is observed that spatial layout of cell structure is inherently wider compared to generic object classes. The aim is to capture vital spatial structure from the cell characteristics by defining wider regions in conjunction with rectangular areas. The regions represent different slices/parts of an input image in horizontal and vertical directions, which are computed from the base feature map itself by means of a region based polling rather than slicing an input image. Following the same fashion, several hierarchical regions are selected at multi-scales from the same base feature map, geometrically implying around the center of an image. In this way, a collection of N regions is formulated from base feature map indicating multiple spatial contexts having different aspect ratios.

For region construction, the output feature map of backbone network is upsampled to a higher spatial dimension ($H \times W$) and intended to build a pair-wise spatiality mapping between actual input-image dimension and upscaled deep feature map. An intrinsic relationship is established between image-parts with allied spatial dimensions of the feature map from which the regions are computed via bilinear pooling. The feature map dimension of each regions is uniform, given as $r_i \in F_i^{h \times w \times C}$. Next, a GAP layer is applied to select

channel-wise features ($1 \times 1 \times C$) from each region, resulting in a total of N regions, denoted as $R \in F^{N \times C}$. To this end, two different groups of non-overlapping regions representing holistic deep feature map are computed with different spatial window sizes. A bigger window-size generates $N=5$ regions, and another group comprises $N=15$ regions having smaller window-size. The number of regions is kept small, considering a low computational budget to formulate a graph with N regions as the nodes.

3.3. Graph Convolutional Network (GCN) With Channel Splitting

Graph convolutional network (GCN), a sub-field of graph neural network (GNN), plays a vital role in modeling of graph structural data Li, Xie, Wan, Lv, Song and Lv (2023b). Graph convolution captures semantic correlation by building spatial relationship between the node features and propagates relevant features of different image-regions, maintaining the gradient flow as well as suppressing vanishing gradient problems. One of the most widely used layer-wise propagation rules for modeling graph-data was devised by Kipf and Welling (2017), which is apposite for semi-supervised node classification. This multi-layer GCN efficiently captures spatial structures while working with images. Herein, Kipf-Welling's formulation of normalized graph Laplacian for defining graph convolution diminishing overfitting problem is applied. Their renormalization method offers an efficient and fast layer-wise propagation of spectral convolutions on graph structures relying on the first-order approximation, called GCN. This GCN is scalable and suitable for graph-based data and broader classes of image classification including histopathology images.

A graph $\mathcal{G} = (\mathcal{N}, \mathcal{E})$ is constructed with \mathcal{N} nodes and \mathcal{E} edges, for deep feature propagation via semantic understanding among the local regions. A GCN is utilized to establish a spatial relation interpreting the features through a graph \mathcal{G} , where the nodes are defined with pooled channel-wise features (C), as described in Sec. 3.2. The graph \mathcal{G} is constructed by an undirected adjacency matrix $\mathbf{A} \in \mathbb{R}^{N \times N}$ to represent node-level interactions. The adjacency matrix $\tilde{\mathbf{A}} = \mathbf{A} + \mathbf{I}_N$ denotes \mathbf{A} with added self-connections and \mathbf{I}_N is the identity matrix. The layer-wise feature propagation is computed as:

$$\mathcal{H}^{(l+1)} = \text{ReLU} \left(\hat{\mathbf{A}} \mathcal{H}^{(l)} \mathcal{W}^{(l)} \right); \mathcal{H}^{(0)} = \mathbf{F}; \quad \mathcal{H}^{(L)} = \mathcal{Y} \quad (2)$$

where $l = 0, 1, \dots, L - 1$ is the number of layers, $\tilde{\mathbf{D}}_{ii} = \sum_j \tilde{\mathbf{A}}_{ij}$, and $\mathcal{W}^{(l)}$ is a weight matrix of the l^{th} layer. Rectified linear unit (ReLU) activation function is denoted by $\sigma(\cdot)$. The symmetrically normalized adjacency matrix is $\hat{\mathbf{A}} = Q \tilde{\mathbf{A}} Q$; and $Q = \tilde{\mathbf{D}}^{-0.5}$ denotes the diagonal node-degree matrix of $\tilde{\mathbf{A}}$. The output \mathcal{Y} with the convoluted features per node.

Now, the region-aware feature vector, denoted as $\mathbf{F}_{N \times C}$ is fed into the first layer of GCN, which captures local neighborhood via aforesaid propagation rule, given as

$$\mathbf{F}^{(k+1)} = \mathcal{H}^{(k)} \left(\mathbf{F}_{N \times C}^{(k)}, \hat{\mathbf{A}}_{N \times N} \right) \quad (3)$$

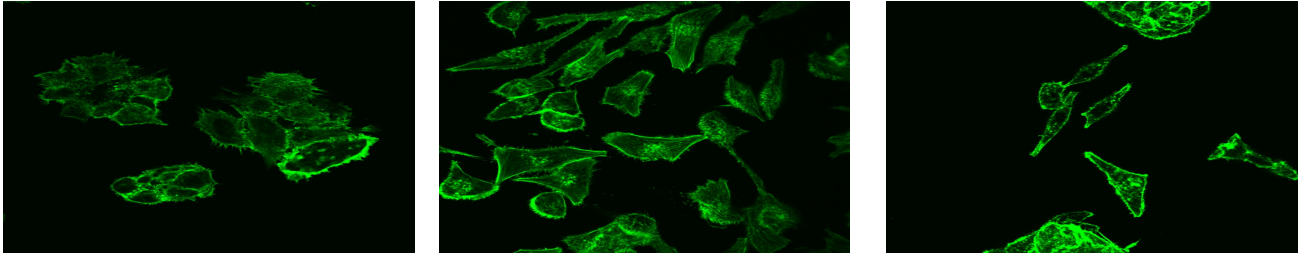


Figure 4: Samples of cell images from the FMID dataset Oei et al. (2019).

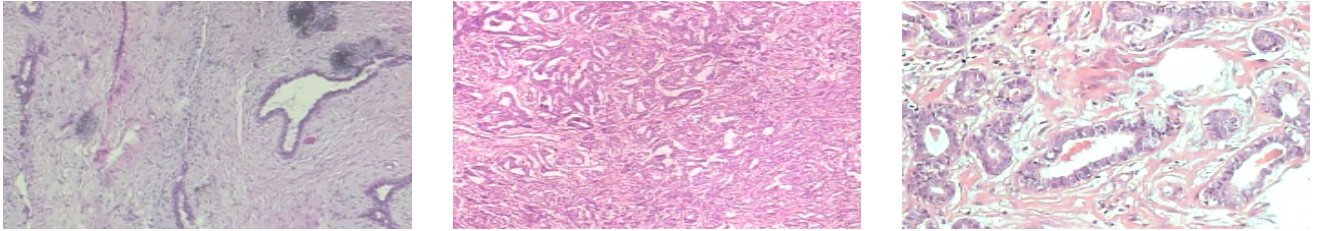


Figure 5: Breast cancer images of the BreakHis dataset Spanhol et al. (2016).

where, $\mathbf{F}^{(k)}$ is the output feature vector of graph convolution at k^{th} layer. Next, the feature maps are pooled along the channel dimension using GMP and GAP layers for selecting discriminative feature maps from these nodes (eq. 4).

$$\mathbf{F}^{(k+2)} = \text{Concat}[\text{MaxPool}(\mathbf{F}^{(k+1)}); \text{AvgPool}(\mathbf{F}^{(k+1)})] \quad (4)$$

Afterward, the channel-wise selected information, i.e., the output of layer $(k+1)$ is $\mathbf{F}^{(k+2)}$, is mixed for determining an efficient feature descriptor, denoted as $\mathbf{F}_{mix} \in \mathbb{R}^{2 \times C}$. The mixed channel descriptors are downsampled for further feature selection and refinement, $\mathbf{F}_{mix} \rightarrow \mathbf{F}_{m'} \in \mathbb{R}^{4 \times C/2}$. This channel-splitting technique is suitable for reducing drastically the number of nodes of a spatial graph structure while preserving the salient features (eq. 5), shown in Fig. 3. As the number of regions could be scaled up, the node level interactions would become more complex, thereby increasing computation cost of applying more layer-wise propagation using GCN. Thus, considering a low computational cost of incurring additional layers in GCN, channel-wise feature splitting is effective for addressing cancer image classification problems.

A few methods built a GCN with comparatively more number of nodes, and then, selected discriminative nodes maintaining the same dimension of node-level features, i.e., channel dimension remains unaltered Bera et al. (2024a). Those techniques overlook channel-wise feature interactions, and the nodes might propagate redundant features,

which are addressed in this work. Essential features are selected via channel-splitting by ignoring less significant others, which in turn reduce model parameters maintaining a high performance. Thus, the CS-GCN offers an efficient feature aggregation.

$$\begin{aligned} \mathbf{F}_{m'} &= \text{Reshape}(\mathbf{F}_{mix}^{4 \times C/2}), \\ \mathbf{F}^{(k+3)} &= \mathcal{H}^{(k+2)}(\mathbf{F}_{m'}, \hat{\mathbf{A}}_{4 \times 4}) \end{aligned} \quad (5)$$

The output feature map of GCN layer-II (eq. 5) is denoted as $\mathbf{F}^{(k+3)}$. It represents a decreased feature space by mixing and reducing channel-wise features, obtained from GCN layer-I (eq. 3). Afterward, an average pooling layer is included to summarize GCN based feature maps. This readout layer aggregates blended and reduced node-level features into a fixed-dimensional feature vector \mathbf{F}_G .

$$\begin{aligned} Y_{pred} &= \text{Softmax}\left(\text{BatchNorm}(F_G)\right), \\ \text{where } F_G &= \text{AvgPool}(\mathbf{F}^{(k+3)}) \end{aligned} \quad (6)$$

The batch normalization (*BatchNorm*) and dropout layers are included in the network for handling the overfitting issues. The final feature vector is passed through a *softmax* layer for estimating probability of the output predicted class-label $\bar{l} \in Y_{pred}$ corresponds to the true class-label $l \in Y$ of object classes Y . The Stochastic Gradient Descent (SGD)

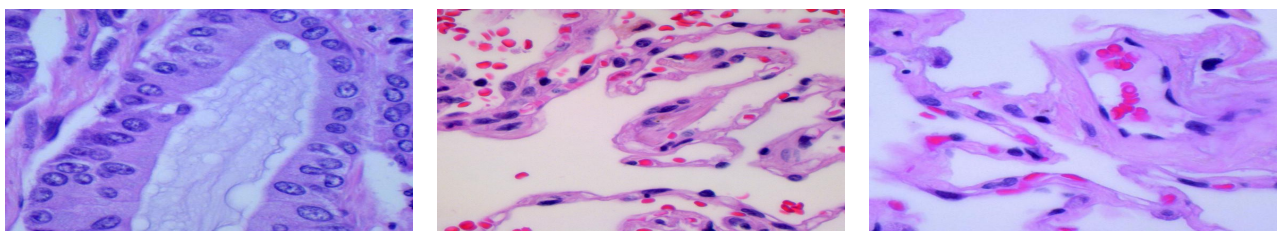


Figure 6: Samples of lung cancer images from the LC25000 dataset Borkowski et al. (2019).

Table 1

Dataset distribution summary with the best Accuracy (%) of CS-GCN(+) .

Dataset	Train: Test	No. Class	Accuracy (Proposed CNN)	Accuracy (ResNet-50)
FMID	402:150	3	97.22	99.30
BreakHis40x	1395:600	8	96.83	98.00
BreakHis100x	1460:621	8	97.43	97.81
BreakHis200x	1415:598	8	97.17	97.33
BreakHis400x	1270:550	8	96.11	96.85
LC25000	17500:7500	5	99.87	100.0

Table 2

Detailed image-level and patient-level specifications of BreakHis Dataset Spanhol et al. (2016).

Subtype / Magnification	40x	100x	200x	400x	Total Images	No. Patients
Benign	652	644	623	588	2480	24
Malignant	1370	1437	1390	1232	5429	58
Adenosis (A)	114	113	111	106	444	4
Fibroadenoma (F)	253	260	264	237	1014	10
Phyllodes Tumor (PT)	109	121	108	115	453	3
Tubular Adenoma (TA)	149	150	140	130	569	7
Papillary Carcinoma (PC)	145	142	135	138	560	6
Ductal Carcinoma (DC)	864	903	896	788	3451	38
Lobular Carcinoma (LC)	156	170	163	137	626	5
Mucinous Carcinoma (MC)	205	222	196	169	792	9
Total	1995	2081	2013	1820	7909	82

optimizer and categorical cross-entropy loss is applied to optimize the learning phase.

The GCN module can be plugged into state-of-the-art (SOTA) base CNNs such as pre-trained ResNet, MobileNet, and others, which are denoted as **CS-GCN+**. Whereas, **CS-GCN** symbolizes the proposed convolutional stem with the same GCN, trained from scratch. Here, both kinds of base CNNs are used alternatively to develop GCN module, denoted as **CS-GCN(+)**.

4. Results and Discussion

The characteristics of datasets are briefed in Table 1, followed by the implementation description and evaluation metrics. The performances are evaluated and compared with SOTA methods, the ablation studies are reported.

4.1. Dataset Description

Three different public datasets are evaluated using the CS-GCN(+). These are (a) human breast epithelial cell lines using actin-labeled fluorescence microscopy image dataset Oei et al. (2019), dubbed as FMID, illustrated in Fig. 4. This tiny dataset consists of one non-cancerous human breast epithelial cell line (MCF-10A) and two cancerous human breast epithelial cell lines (MCF-7 and MDA-MB-231). The MCF-7 is less aggressive and MDA-MB-231 is more aggressive cancer cell lines, respectively.

(b) The BreakHis dataset consists of 7909 images representing four magnification types i.e., 40x, 100x, 200x, and 400x Spanhol et al. (2016). The sub-types are adenosis (A), fibroadenoma (F), phyllodes tumor (PT), and tubular adenoma (TA); and four malignant tumors (breast cancer): ductal carcinoma (DC), lobular carcinoma (LC), mucinous

carcinoma (MC) and papillary carcinoma (PC). This dataset has been widely studied in many works due to its higher clinical value. Detailed sub-class specifications of image-level and patient-level are given in Table 2. Samples of BreakHis 40x and 100x magnifications are shown in Fig. 5. (c) The LC25000 represents histology images of benign and cancerous lung and colon cancer, shown in Fig. 6 Borkowski et al. (2019). This balanced dataset contains a total 25000 images of five classes with 5000 images per class. The classes are colon adenocarcinoma, benign colon tissue, lung adenocarcinoma, lung squamous cell carcinoma, and benign lung tissue.

The experiments are conducted with a train-test ratio of 70:30 for multi-class categorization. Other splitting ratios of datasets and evaluation strategies (e.g., binary classification with 80:20 ratio) are avoided for a fair comparative study with SOTA methods. A summary of these datasets alongside the best results achieved by the proposed CNN stem (CS-GCN) and ResNet-50 (CS-GCN+) are given in Table 1.

4.2. Implementation Specification

The proposed CNN stem is trained from scratch (random initialization), whereas pre-trained *ImageNet* weights are used for initializing the standard base CNNs e.g., ResNet-50, DenseNet-201, etc. During pre-processing, affine transformations are applied. The input images are resized to 224×224 dimension. Image augmentation methods, particularly random rotation (± 25 degrees), scaling (± 0.25), and translation are applied on-the-fly for data diversity. The output feature map of a base CNN is 4×4 pixels and channels=2048, which is upsampled to 32×32. The size of each region is set to 16×16 pixels for $N = 5$ and 48×48 for $N = 15$. A dropout rate of 0.3 is applied to ease overfitting. The

Table 3

Performance evaluation of the CS-GCN with N=5 nodes based on the proposed CNN Stem, and + GCN implies CS-GCN.

Dataset	Method	Top-1 Acc	Top-3 Acc	Precision	Recall	F1-Score
FMID	CNN Stem Baseline	84.02	96.0	86.0	84.0	85.0
	+ 5 Regions	94.02	99.0	94.0	94.0	94.0
	+ GCN	96.52	100.0	97.0	97.0	97.0
BreakHis 40x	CNN Stem Baseline	87.50	96.50	88.0	88.0	88.0
	+ 5 Regions	92.00	98.67	92.0	92.0	92.0
	+ GCN	96.16	99.70	96.0	96.0	96.0
BreakHis 100x	CNN Stem Baseline	85.73	94.50	90.0	86.0	88.0
	+ 5 Regions	92.23	99.20	94.0	94.0	94.0
	+ GCN	95.99	99.50	96.0	96.0	96.0
BreakHis 200x	CNN Stem Baseline	83.76	96.83	84.0	84.0	84.0
	+ 5 Regions	87.33	97.86	89.0	87.0	88.0
	+ GCN	92.33	98.75	93.0	93.0	93.0
BreakHis 400x	CNN Stem Baseline	84.44	95.30	84.0	84.0	84.0
	+ 5 Regions	89.25	95.66	89.0	89.0	89.0
	+ GCN	92.40	99.62	92.0	92.0	92.0
LC 25000	CNN Stem Baseline	64.50	95.0	83.0	75.0	79.0
	+ 5 Regions	92.78	96.0	93.0	93.0	93.0
	+ GCN	93.96	98.0	94.0	94.0	94.0

Table 4

Performance of CS-GCN(+) using the proposed stem and base CNNs with 15 nodes (N). The best top-1 accuracies are shown in bold font and the top-1 accuracies attained by the proposed CNN are underlined.

Dataset	Method	Top-1 Acc	Top-3 Acc	Precision	Recall	F1-Score
FMID	Proposed CNN	<u>97.22</u>	100.0	97.0	97.0	97.0
	ResNet-50	99.30	100.0	99.0	99.0	99.0
	DenseNet-201	100.0	100.0	100.0	100.0	100.0
	MobileNet-v2	95.83	100.0	96.0	96.0	96.0
BreakHis 40x	Proposed CNN	<u>96.83</u>	99.83	96.0	96.0	96.0
	ResNet-50	98.00	99.83	98.0	98.0	98.0
	DenseNet-201	97.33	99.83	97.0	97.0	97.0
	MobileNet-v2	96.50	99.83	97.0	97.0	97.0
BreakHis 100x	Proposed CNN	<u>97.43</u>	99.48	97.0	97.0	97.0
	ResNet-50	97.81	99.70	98.0	98.0	98.0
	DenseNet-201	97.78	99.83	97.0	97.0	97.0
	MobileNet-v2	96.47	99.10	96.0	96.0	96.0
BreakHis 200x	Proposed CNN	<u>97.17</u>	99.50	97.0	97.0	97.0
	ResNet-50	97.33	99.83	97.0	97.0	97.0
	DenseNet-201	95.83	99.90	96.0	96.0	96.0
	MobileNet-v2	97.00	99.78	97.0	97.0	97.0
BreakHis 400x	Proposed CNN	<u>96.11</u>	99.44	96.0	96.0	96.0
	ResNet-50	96.85	100.0	97.0	97.0	97.0
	DenseNet-201	96.48	99.44	96.0	96.0	96.0
	MobileNet-v2	94.63	99.26	95.0	95.0	95.0
LC 25000	Proposed CNN	<u>99.87</u>	100.0	100.0	100.0	100.0
	ResNet-50	100.0	100.0	100.0	100.0	100.0
	DenseNet-201	100.0	100.0	100.0	100.0	100.0
	MobileNet-v2	99.67	100.0	100.0	100.0	100.0

model is trained with a learning rate of 0.005 for 400 epochs and with a mini-batch size of 12. The model parameters are calculated in millions (M). The CS-GCN method is developed in Tensorflow 2.x and Keras 2.13.x using Python scripts. For experiments, a NVIDIA A100 40GB GPU and Intel Core Silver 4316 CPU x86_64, 2.30 GHz 128 GB RAM computing system are used.

4.3. Evaluation Metrics

The top-1 and top-3 accuracy, precision, recall, and F1-score (eq. 7) metrics are computed for performance evaluation and comparison. These metrics are widely used in prior works to tackle class imbalance problem. Also, patient-level metrics are used for evaluating the BreakHis (BH) dataset according to the benchmark.

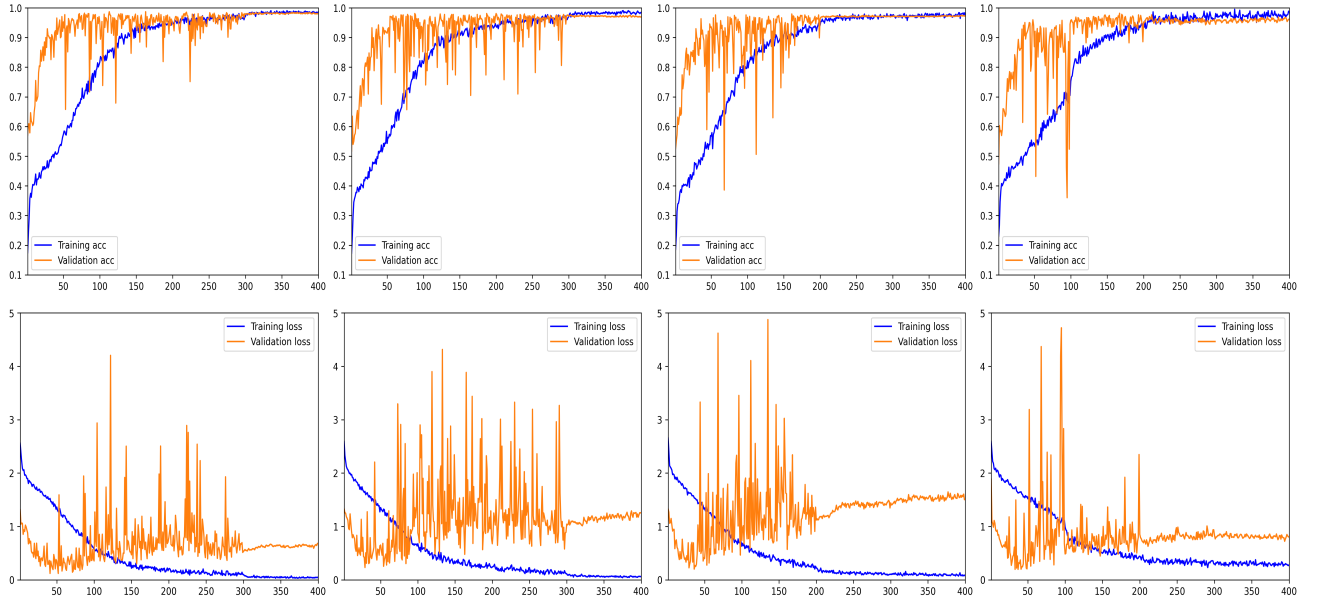


Figure 7: Accuracy (top-row) and loss (bottom-row) during training and testing of CS-GCN with 15 nodes built upon ResNet-50 on the BreakHis four magnifications are shown from the left to right: 40x, 100x, 200x, and 400x, respectively.

$$\begin{aligned}
 \text{Accuracy} &= \frac{\mathcal{TP} + \mathcal{TN}}{\mathcal{TP} + \mathcal{TN} + \mathcal{FP} + \mathcal{FN}} \\
 \text{Precision} &= \frac{\mathcal{TP}}{\mathcal{TP} + \mathcal{FP}} \\
 \text{Recall} &= \frac{\mathcal{TP}}{\mathcal{TP} + \mathcal{FN}} \\
 \text{F1-Score} &= 2 \times \frac{\text{Precision} \times \text{Recall}}{\text{Precision} + \text{Recall}}
 \end{aligned} \tag{7}$$

where \mathcal{TP} denotes the number of true positives, \mathcal{TN} is the number of true negatives, \mathcal{FP} is the number of false positives, and \mathcal{FN} is the number of false negatives.

The image-level and patient-level performance metrics are evaluated for cancer classification as defined by Spanhol et al. (2016). The accuracy of patient-level is assessed as the patient recognition rate (PRR). Let the number of cancer images of a patient K is K_p , the number of images classified correctly is K_{rec} , and N be the number of total patients. The PRR is defined as

$$\text{PRR} = \frac{1}{N} \sum_{K=1}^N \frac{K_{rec}}{K_p} \tag{8}$$

The patient-level performance of CS-GCN is assessed on the BreakHis dataset following similar evaluation metrics Zou, Chen, Che, Zhang and Zhang (2022), given in Table 7.

The image-level classification accuracy is mainly computed here due to its wider acceptability by the researchers. Let N_{total} be the number of all cancer images in the testing set, and N_c defines the number of images correctly classified, then the image recognition rate (IRR) is given as

$$\text{IRR} = \frac{N_c}{N_{total}} \tag{9}$$

The performances are evaluated on different datasets according to aforesaid metrics, described next.

4.4. Performance Analysis

Firstly, baseline performance of the proposed CNN stem is computed. Then, the performance of five regions ($N=5$) added on base CNN is evaluated. Lastly, the GCN module is integrated with the model to develop CS-GCN. Detailed performances showcasing baseline results on all datasets using proposed CNN and its integration with $N=5$ nodes in GCN layer-I are provided in Table 3. It is evident that the performances are improved progressively with the added GCN module. For example, the baseline accuracy of the proposed stem is 87.50%, which is improved to 92.0% with 5 regions, and GCN further enhances the accuracy to 96.16% on BreakHis 40x. Overall performances are satisfactory while evaluated using the proposed convolutional stem. To improve further, the number of regions is increased ($N=15$) for enhancing local contextual representation and selecting more discriminatory information. The best performances are attained with $N=15$ nodes in layer-I of GCN and overall results are showcased in Table 4. The model parameters are given in Table 5.

Besides, many prior works utilized available backbone families, such as ResNet-50, DenseNet-201, etc. and those are compared in Table 6. Here, experiments are conducted with three standard base CNNs upon which the GCN module is plugged-in. Particularly, more region-aware features with increased regions are learned through pre-trained backbones which have boosted the performances. The most significant results of CS-GCN(+) are demonstrated in Table 4. The top-1 accuracy (%) of CS-GCN on each dataset is underlined and the best top-1 accuracy of CS-GCN+ is denoted with boldface. For example, CS-GCN attains 96.83% accuracy using our backbone and 98.0% accuracy using ResNet-50 on BreakHis 40x. The results exhibit that performances of base stem are competitive with pre-trained CNNs, even having a low model complexity than ResNet-50 and DenseNet-201.

Table 5

Model parameters of the CS-GCN(+) are estimated in millions (M) and underlined those models are < 10M.

Model	Proposed CNN	ResNet-50	DenseNet-201	MobileNet-v2
Baseline	<u>7.92</u>	23.60	18.34	<u>2.28</u>
CS-GCN	13.15	28.85	25.10	<u>5.94</u>

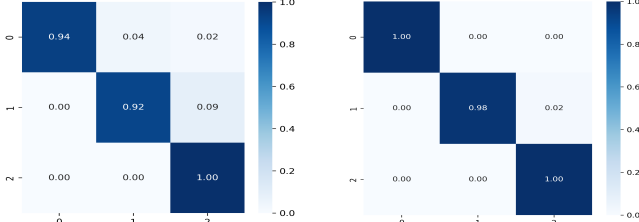


Figure 8: Confusion matrix of CS-GCN based on the proposed CNN (left) and ResNet-50 (right) on the FMID dataset.

The accuracy and loss graphs of training and testing phases of CS-GCN+ using ResNet-50 base on all four magnifications of BreakHis dataset are shown in Fig. 7. The graphs (top-row) exhibit very similar behaviors during evaluations and the estimated loss values are shown in bottom-row. Particularly, the training has stabilized after 300 epochs for all four scenarios. Similar behavior has been observed in other datasets too.

Patient-level performances of CS-GCN+ with $N=15$ nodes are computed on the BreakHis dataset, and the results are provided with a comparative study in Table 7. The accuracy on the BreakHis 40x is 97.40 ± 0.4 using ResNet-50, and similar accuracy on other magnifications are obtained accordingly. The accuracy of the proposed CNN is competitive with pre-trained backbones. A patient-level performance comparison is presented in the next section.

Model parameters of the proposed stem is 7.92M and full CS-GCN is 13.15M, which is very low compared to ResNet-50 and DenseNet-201 backbones. The proposed CNN is comparable to lightweight MobileNet-v2 comprises 2.28M parameters. Hence, the developed stem is considered to be a lightweight model having < 10M parameters. Notably, CS-GCN implemented using MobileNet-v2 consists of 5.94M parameters, which is still a lightweight model.

The CS-GCN is a good choice while targeting a lower computational cost, yet powerful to attain SOTA results. The reason could be that standard CNNs are pre-trained on generic image classes, which always might not be a good choice for medical diagnostics, representing very complex patterns/textures and cell structures. To overcome this problem, many works ensembled multiple CNNs, ignoring computational cost. To avoid such a huge parametric overload of fusion-based models, CS-GCN is an effective alternative.

4.4.1. Visualizations

The confusion matrix of CS-GCN+ ($N=15$) on each dataset is shown in Fig 8, 9, 10, and 11 for visual clarity of evaluation. The t-distributed stochastic neighbor embedding (t-SNE) visualizations exhibit data separability in different

clusters of classes Van der Maaten and Hinton (2008). Similar data points represent small pairwise distances, while different data points imply large pairwise distances using student-t distribution. Here, low-dimensional feature distributions reflect the discriminability of multiple classes using CS-GCN. The t-SNE plots (Fig. 12) show class-wise feature distributions captured by CS-GCN built with ResNet-50.

The gradient weighted class activation mapping (Grad-CAM) visualizations reflect a deep model's capacity in coarse localizing crucial regions within input image for prediction without altering architectural design Selvaraju, Cogswell, Das, Vedantam, Parikh and Batra (2017). Grad-CAM utilizes gradient information flowing into the last convolutional layer of a CNN to estimate the neuron-level importance for making a prediction. Grad-CAM is widely used for class-discriminative visual explanation with high resolution details and interpretability which are useful for decision making. These superimposed visual analyses, shown in Fig. 13, clearly showcase overall feature representations of the vital region of interests which are relevant for classification of cancer images using CS-GCN(+).

4.5. Performance Comparison

The performances are compared with existing SOTA for multi-classification (Table 6), considering similar evaluation techniques like ours. A knowledge distillation based joint learning (student-teacher) framework achieved a classification accuracy of 97.23% and 96.92% on the BreakHis 40x and 100x magnifications, respectively Sepahvand and Abdali-Mohammadi (2023). A small squeeze-and-excitation block combined with a residual module, called breast cancer histopathology image classification network (BCHNet), trained with a Gaussian error scheduler (ERF), attained 94.43% accuracy on multi-classification on this dataset Jiang et al. (2019). In contrast, CS-GCN attains improved results on these magnifications. The best performances of CS-GCN+ are 98.0% and 97.81% using ResNet-50, on the BreakHis 40x and 100x, respectively, implying a distinct accuracy gain. Likewise, the accuracies of CS-GCN+ using ResNet-50 on BreakHis 200x (97.33%) and 400x (96.85%) are improved over an embedded fusion mutual learning (EFML) method that reported 96.65% and 96.41% accuracies on the BreakHis 200x and 400x, respectively Li et al. (2023a). The performance of using proposed stem in CS-GCN outperforms several existing methods, and its effectiveness is competitive with those methods built with ResNet-50. The CS-GCN attains better performances than MobileNet-V2 (Table 4). A modified VGG-16 network with naive inception blocks (VGGIN-Net) reported an average accuracy of 95.81% on this dataset Saini and Susan (2023).

Graph Convolutional Network With Channel Splitting for Cancer Classification

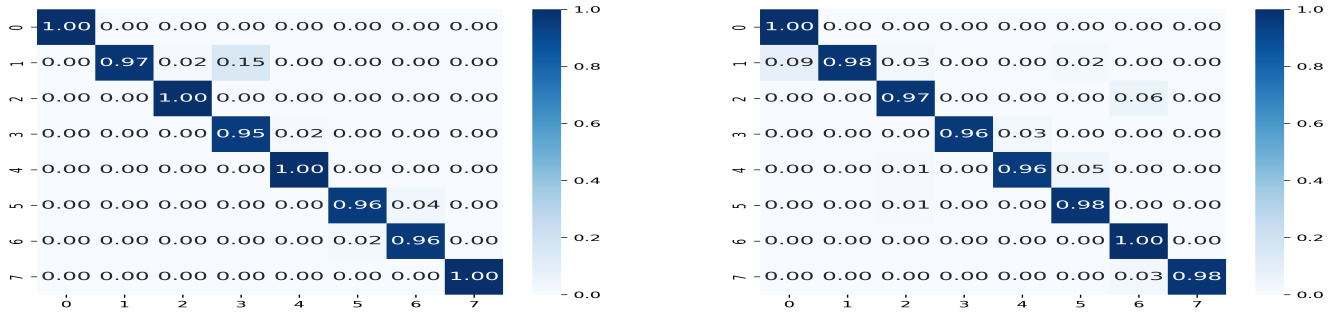


Figure 9: Confusion matrix evaluated using ResNet-50 on the BreakHis 40x (left) and BreakHis-100x (right) magnifications.

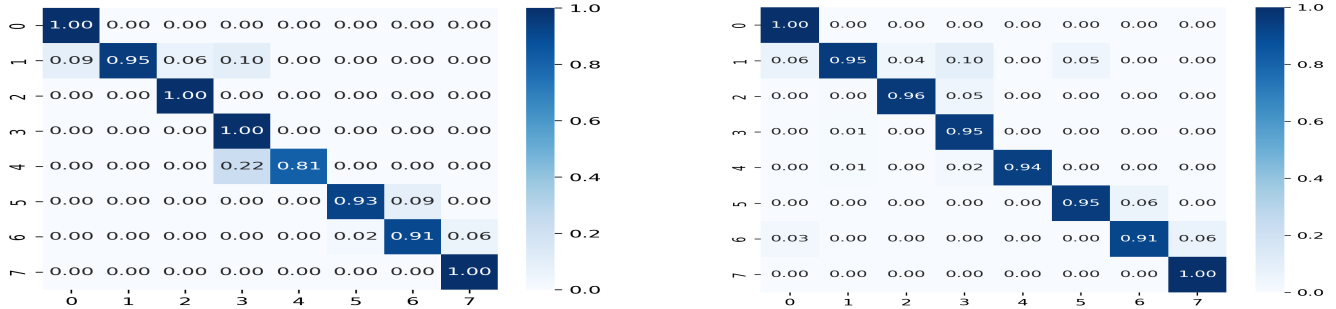


Figure 10: Confusion matrix evaluated using the proposed CNN on BreakHis 200x (left), and ResNet-50 on BreakHis 400x (right) magnifications.

A collaborative transfer network (CTransNet) achieved the best 98.21% accuracy on BreakHis 40x magnification with 224×224 image size, whereas the average accuracy of all four magnifications is 97.39% Liu, Wang, Zhang, Qiao, Sun, Zhang, Xu and Shang (2024a). Recently, an improved DenseNet model, called DinNet, was tested with 80:20 train-test ratio, and achieved 97.62% average accuracy Guo et al.

(2024). However, CS-GCN has attained 97.50% average accuracy with 70:30 train-test ratio. Reasonably, this experimental setting is not directly comparable with those existing methods due to dissimilar experimental setup, yet CS-GCN achieves competitive performances. The dependency-based lightweight convolutional neural network (DBLCNN) Wang et al. (2022), built upon MobileNet-V2 with 12.19M

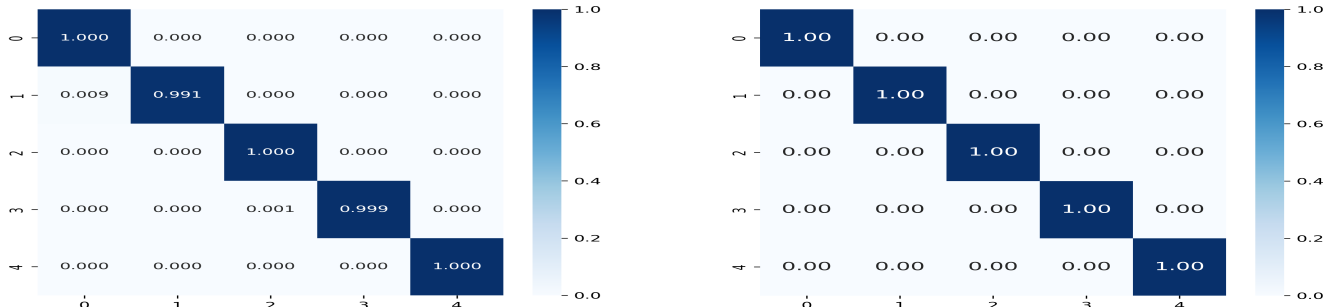


Figure 11: Confusion matrix of CS-GCN computed using the proposed CNN (left) and ResNet-50 (right) on LC25000 dataset.

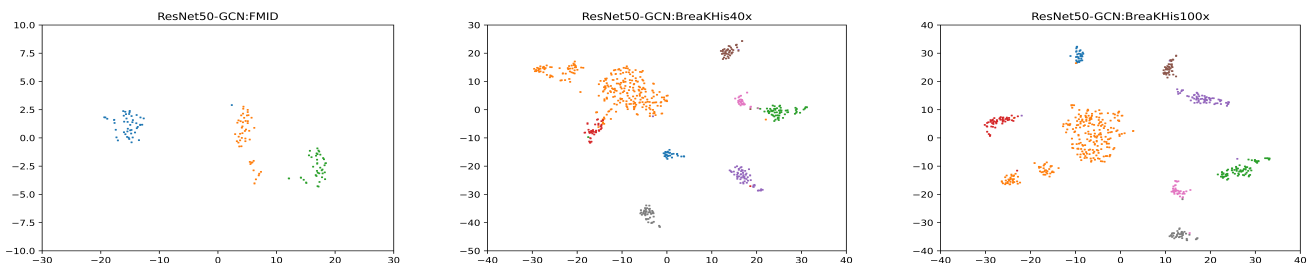


Figure 12: t-SNE plots of proposed CS-GCN(+) using ResNet-50 on the FMID (left), BreakHis 40x (mid) and BreakHis 100x (right) magnifications.

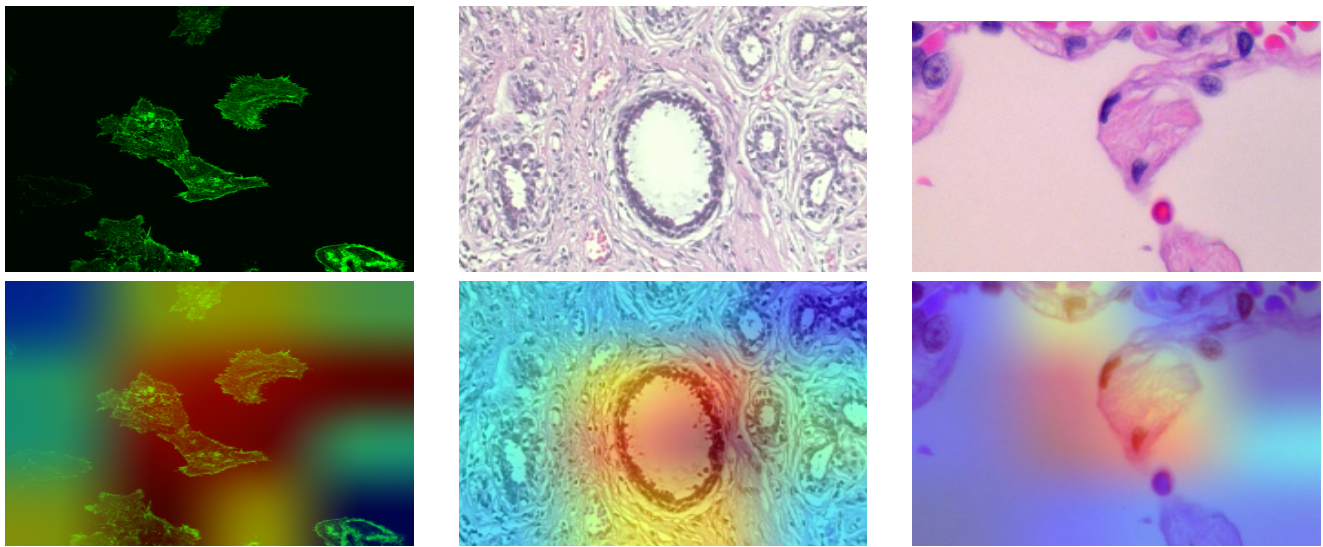


Figure 13: Grad-CAM visualizations using the proposed method on the FMID (left), BreakHis 100x (mid) and LC25000 (right) datasets are shown in bottom row with the corresponding actual image given in top-row.

Table 6

Image-level accuracy (%) comparison with SOTA on the BreakHis (BH) 40x, 100x, and average (Avg) of all four magnifications.

Method	BH 40x	BH 100x	Avg
BHCNet +ERF Jiang et al. (2019)	94.43 ± 0.28	94.45 ± 0.15	
Hybrid harmonization Abdallah, Marion, Tauber, Carlier, Hatt and Chauvet (2023)	93.40	-	
CSDCNN Han, Wei, Zheng, Yin, Li and Li (2017)	92.80 ± 2.1	93.90 ± 1.9	
Semantic dual contrast Liu, Zhu, Gu, Pan, Li, Fan, Li and Zeng (2024b)	95.70	94.50	95.40
Ensemble of Swin Transformers Tummala et al. (2022)	96.00	92.60	
Embedded fusion mutual learning (EFML) Li et al. (2023a)	96.76	97.36	
VGGIN-Net Saini and Susan (2023)	96.28	96.81	95.81
DBLCNN Wang, Gong, Cheng and Qian (2022)	96.58	95.65	96.00
CS-GCN+ (ResNet-50 + GCN)	97.43 ± 0.57	97.60 ± 0.21	97.50
CS-GCN (proposed CNN + GCN)	96.33	97.43	96.88

parameters, achieved an average 96.00% accuracy of image classification on BreakHis. In contrast, CS-GCN based on MobileNet-V2, having 5.94M parameters, has attained an average of 96.15% classification accuracy.

Patient-level multi-classification performance of the proposed CS-GCN on the BreakHis dataset is compared with SOTA. The accuracy of class structure-based deep convolutional neural network (CSDCNN) on augmented BreakHis 40x is $94.1 \pm 2.1\%$ Han et al. (2017). A multi-level feature fusion (MLF2) method using pretrained CNN has gained $95.2 \pm 2.4\%$ accuracy of patient-level assessment on the

BreakHis 40x, and similar results on other magnifications are reported Taheri et al. (2024). An inception recurrent residual convolutional neural network (IRRCNN) adapting data augmentation obtained 96.76 ± 1.1 accuracy on BreakHis 40x Alom et al. (2019). In contrast, CS-GCN attains at least 97.0% patient-level accuracy in similar experiments on this sub-dataset. Though, several methods evaluated binary performances and attained more than 99% accuracy, which are avoided for comparison due to dissimilar experimental setup, as mentioned above.

Table 7

Patient-level performance of CS-GCN(+) on four magnifications of the BreakHis (BH) dataset and comparison with SOTA.

method/CNN	BH 40x	BH 100x	BH 200x	BH 400x
CSDCNN Han et al. (2017)	94.1 ± 2.1	93.2 ± 1.4	94.7 ± 3.6	93.5 ± 2.7
MLF2-CNN Taheri, Golrizkhataami, Basabbrain and Hazzazi (2024)	95.2 ± 2.4	95.8 ± 1.5	95.6 ± 1.9	95.1 ± 1.9
RANet Zhou, Zhang and Gao (2022)	92.21	97.50	97.83	89.73
DSoPN Li, Zhang, Sun, Zhang, Dong, Che and Zhang (2020)	95.01	96.84	97.92	96.28
IRRCNN Alom et al. (2019)	96.76 ± 1.1	96.84 ± 1.1	96.67 ± 1.3	96.27 ± 0.9
CS-GCN+ (ResNet-50 + GCN)	97.40 ± 0.4	97.46 ± 0.3	97.81 ± 1.4	96.74 ± 1.1
CS-GCN+ (MobileNet-V2 + GCN)	97.55	97.23	96.75	95.06
CS-GCN (proposed CNN + GCN)	97.00	97.29	97.52	96.12

Table 8

The baseline accuracy of using base CNNs and added regions (N)

Method	FMID	BreakHis 40x	BreakHis 100x	BreakHis 200x	BreakHis 400x	LC25000
ResNet-50 Baseline +15 Regions	79.17	78.83	76.28	81.00	77.22	95.75
	90.26	92.16	91.02	94.00	92.40	97.93
DenseNet-201 Baseline +15 N	81.23	80.00	77.40	80.83	80.18	95.16
	92.36	85.50	83.33	93.66	87.40	97.80
MobileNet-v2 Baseline +15 Regions	78.47	68.50	65.38	73.50	76.48	94.68
	90.93	85.16	91.34	93.00	91.48	96.98

Table 9

Ablation study (Sec.4.6.c) with GCN Layer-I=2048 and Layer-II=1024 features in the CS-GCN(+); 512 denotes GCN Layer-II=512; $5N^{(1L)}$ denotes 1 layer GCN with 5 nodes (1st row) while remaining all GCNs built with 2 layers; followed by the feature size of GCN Layer-II in 2nd column.

Method	Nodes; Feat.	FMID	BH40x	BH100x
Proposed CS-GCN	$5N^{(1L)}$; 1024	92.36	93.53	90.38
	5 N; 1024	96.52	96.16	95.99
ResNet50 MobNetv2	5 N; 1024	96.87	96.46	96.07
	5 N; 1024	96.44	94.33	94.91
CS-GCN	15 N; 512	97.00	97.10	96.15
	15 N; 512	97.22	96.50	96.31
	15 N; 512	96.52	96.00	95.66
CS-GCN	15 N; 1024	97.22	96.50	96.47
	15 N; 1024	97.91	95.16	97.11
	15 N; 1024	96.83	96.16	96.15

An ensemble of CNNs reported 99% precision for classifying breast epithelial cell dataset (FMID) Maurya et al. (2021). A CNN following VGG-16 model achieved 97.20% accuracy using transfer learning Oei et al. (2019). In contrast, CS-GCN+ using DenseNet-201 has achieved 100% performance, given in Table 4. The top-1 accuracy is 99.30% of CS-GCN+ using ResNet-50. Also, CS-GCN built with proposed stem achieves 97.22% accuracy on FMID.

The MicrosMobiNet architecture developed for mobile-edge computing devices attained 96.52% accuracy and 91.30% F1-score on the LC25000 dataset Biswas and Barma (2024). Condorcet's Jury Theorem-based ensemble method attained 99.88% accuracy on the same dataset for multi-classification of lung and colon cancer Srivastava, Chauhan and Pradhan (2023). Also, a pyramidal deep-broad learning (PDBL) method achieved 99.91% using ResNet-50 on the LC25000 dataset Lin, Han, Pan, Liu, Chen, Li, Jia, Shi, Wang, Cui et al. (2022). An EFML scheme achieved 99.89% average classification result and the best 100% on this dataset Li et al. (2023a). Another work has attained 99.68% accuracy of lung-cancer classification by integrating the DenseNet-201, color histogram, and k-nearest neighbors (kNN) classifiers Noaman, Kanber, Smadi, Jiao and Alsmadi (2024). Likewise, CS-GCN+ attains 100% accuracy using both ResNet-50 and DenseNet-201 backbones (Table 4). Overall, a comparative study with recent SOTA works on three datasets implies that CS-GCN, having 13.15M parameters, improves the performances using proposed lightweight convolutional stem, which is built with only 7.92M parameters.

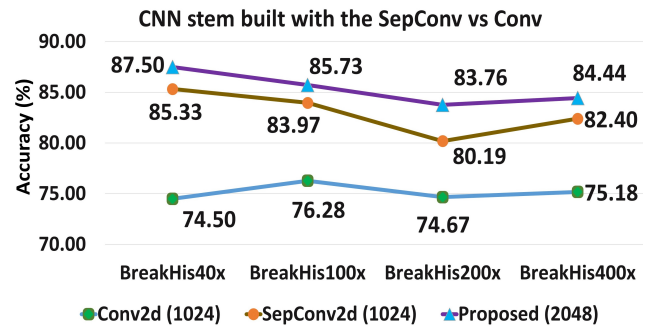


Figure 14: Comparative study (Sec.4.6.a) on the base convolutional stem built with Separable convolutions (*SepConv2D*), and conventional convolutions (*Conv2D*).

The performances using ResNet-50 and other base CNNs have boosted multi-class categorization of breast and lung-colon cancers, and achieved SOTA results, implying the benefits of devised CS-GCN(+).

4.6. Ablation Study

The ablation studies are conducted to explore the significance of the major components of CS-GCN.

(a) The baseline results of CNN stem are evaluated considering three different design variations. The results are comparatively shown in Fig. 14. The CNN stem configuration of [128, 256, 512, 1024] is considered using conventional convolutions and separable convolutions in two different experiments, denoted as *Conv2d(1024)* and *SepConv2d(1024)*, respectively. Next, the stem-depth is increased with [128, 256, 512, 768, 1024, 2048] configuration using *SepConv2d*, denoted as ‘proposed (2048)’ in Fig. 14. Clearly, it is evident that the proposed stem with 2048 filter-sizes enhances baseline performances on all four magnifications of BreakHis with reasonable model parameters. The model parameters are 19.30M for *Conv2d(1024)*, whereas it is 2.18M for *SepConv2d(1024)*. Finally, the proposed stem i.e., *SepConv2d(2048)* is built with 7.92M, and performs better than the other two CNN stem architectures.

(b) Five complementary regions are integrated for region pooling. Finally, the GCN layers are included with $N=5$ for performance improvement. The results of this study are given in Table 3. Likewise, the baseline performance of standard CNNs including 15 regions has been computed, and the results are given in Table 8. The baselines and regions progressively improve the performances which are obvious in network design.

Table 10

Ablation study (Sec.4.6.d): Only max-pooling is applied in CS-GCN instead of concatenation of max and average pooling.

CNN	FMID	BreakHis 40x	BreakHis 100x	BreakHis 200x	BreakHis 400x
Proposed CNN	96.53	95.33	96.63	96.50	95.55
ResNet-50	97.22	96.33	95.91	96.66	94.62
DenseNet-201	97.22	97.17	96.63	94.50	95.41
MobileNet-V2	95.14	95.66	95.15	93.66	92.40

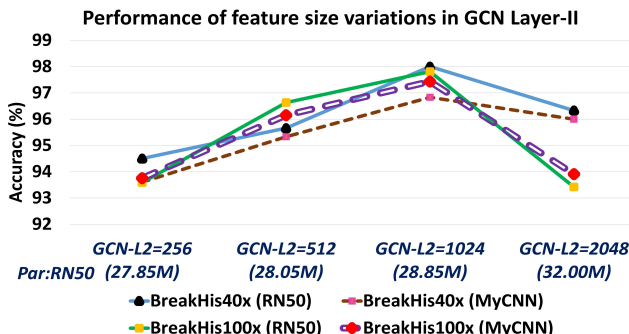


Figure 15: Comparative study (Sec.4.6.c) on different feature sizes in the GCN layer-II using ResNet-50. The model parameters with respective feature spaces are given.

Table 11

Ablation study (Sec.4.6.e) with GCN Layer-I=2048 only followed by the classification avoiding the channel splitting.

Method/CNN	Nodes	FMID	BH40x	BH100x
CS-GCN	5	94.66	93.83	90.16
ResNet-50	5	94.66	94.33	90.80
MobileNet-V2	5	94.00	94.16	90.64
CS-GCN	15	96.00	95.66	93.38
ResNet-50	15	96.66	95.83	93.54
MobileNet-V2	15	96.00	95.50	93.06

(c) The effectiveness of feature propagation in GCN layers with $C=1024$ features per node is studied, and the results are given in Table 9. It is observed that reducing node-level features aggressively discards relevant information, and results in performance degradation. Output of base CNN stem is the same 1024 feature dimension in GCN layer-I for designing the network that provides satisfactory results, given in the first-row of Table 9. The performance of $N=5$ region is studied which implies the need of more regional information for graph-based feature representation.

The performances with variations of feature dimension in GCN layer-II are studied, as shown in Fig. 15. In this study, layer-I contains 2048 features, whereas, channel-splitting module is varied with 256, 512, 1024, and 2048 features using ResNet-50. The results on BreakHis 40x and 100x magnifications clearly show that SOTA performances are achieved with the feature size 1024 in GCN layer-II of CS-GCN(+). Hence, a two-layer GCN with $N=15$ nodes, and $C=2048$ features per node in layer-I and 1024 features in layer-II of GCN is the best performer in present context.

(d) An ablation study is conducted to justify the feature pooling using both GMP and GAP in the GCN module is beneficial than using standalone GMP. The results are provided in Table 10. An average accuracy of 96.0% is attained

by CS-GCN using only GMP built upon proposed CNN on BreakHis dataset considering all magnifications. In contrast, using both GAP and GMP in similar experiments, an average accuracy of 96.88% has been achieved. Likewise, similar gains in performances are achieved using other CNNs on other dataset variations. It implies that feature mixing using both pooling enhances overall feature representation through the graph-nodes of CS-GCN.

(e) The experiments are carried out with only one layer GCN excluding the channel-splitting module (i.e., GCN layer-II) from the model. Both $N=5$ nodes and $N=15$ nodes in GCN-model are tested in different experiments, and the results are provided in Table 11. It is evident that 95.83% accuracy has been attained on BreakHis 40x using ResNet-50 in this experimental study, whereas the best 98.00% accuracy is achieved by CS-GCN+ full model with ResNet-50 (Table 4). It is evident that the accuracy has been degraded excluding channel-splitting module, indicating the module indeed boosts the performances.

4.7. Clinical Applications and Limitations

In recent time, deep learning approaches has achieved remarkable success in various clinical applications including breast cancer diagnosis, classification of histopathological sub-types, lymph node metastasis, and others Zhao, Bai, Guo, Ren and Zhang (2023). Also, visualizations using Grad-CAM showcase qualitative explanations for better diagnostics which are suitable for early detection of cancer and prognosis. Automated methods leveraging machine/deep learning are inexpensive compared to manual time-consuming pathological lesion/biopsy sample collection, testing, and analysis. To mitigate errors in decision making of automated cancer sub-type determination, experts' diagnosis decisions could be combined. Recent integration of large language models (LLMs) in medical applications, multi-modal deep learning and data fusion approaches will improve the correctness in medical reasoning and personalized treatment in rural areas. Thus, integration of vision-language models (i.e., pre-trained CNNs + GPT models) offers a huge potential in cancer patient-care and low-cost clinical applications. However, due to limited training data, advanced preprocessing techniques are yet to be developed for further progress. Generalized deep learning models should be developed for avoiding biases, and addressing data imbalance issues which are major challenges.

Currently, the proposed GCN requires a large number of model parameters (0.42M) per layer, which is computationally expensive in the context of a lightweight CNN design. To overcome this limitation, further improvement is

essential for reducing intrinsic model parameters of GCN for a real-world clinical application as well as lightweight model development. Other types of imaging modalities and data collection from various nations should be carried out for generalizing the model's performance, which is considered as an important future direction.

5. Conclusion

In this paper, a two-layer GCN integrated upon a CNN stem, called CS-GCN, is proposed for cancer multi-class categorization using histopathology and actin-labeled fluorescence microscopy images. The performances are evaluated using three standard backbone CNNs. A new CNN stem is proposed considering a lower computational cost of the network architecture upon which the GCN layers are integrated. The CS-GCN is computationally lightweight compared to standard base CNNs including the ResNet, DenseNet, and other heavier backbone families. Yet, the performance of the developed shallower CNN is competitive with those standard backbones. The performances of CG-GCN on three public cancer datasets using both types of CNNs are improved adeptly compared to existing works. A new fusion strategy using GCN-based deep models will be tested on other datasets on different types of cancers to boost the performance of CAD-based medical diagnosis.

Acknowledgements

This work is supported by the Cross-Disciplinary Research Framework (CDRF: C1/23/168) and New Faculty Seed Grant (NFSG/23-24) projects, and necessary computational infrastructure at the Birla Institute of Technology and Science (BITS) Pilani, Pilani Campus, Rajasthan, 333031, India. This work has been also supported in part by the project (2024/2204), Grant Agency of Excellence, University of Hradec Kralove, Faculty of Informatics and Management, Czech Republic. This work is also supported in part by Long-Term Conceptual Development of Research Organization (2024) at Skoda Auto University, Czech Republic.

References

- Abbas, S.F., Le Vuong, T.T., Kim, K., Song, B., Kwak, J.T., 2023. Multi-cell type and multi-level graph aggregation network for cancer grading in pathology images. *Med. Img. Analysis* 90, 102936.
- Abdallah, N., Marion, J.M., Tauber, C., Carlier, T., Hatt, M., Chauvet, P., 2023. Enhancing histopathological image classification of invasive ductal carcinoma using hybrid harmonization techniques. *Scientific Reports* 13, 20014.
- Abdulaal, A.H., Valizadeh, M., Amirani, M.C., Shah, A.S., 2024. A self-learning deep neural network for classification of breast histopathological images. *Biomedical Signal Processing and Control* 87, 105418.
- Almaslukh, B., 2024. A reliable breast cancer diagnosis approach using an optimized deep learning and conformal prediction. *Biomedical Signal Processing and Control* 98, 106743.
- Alom, M.Z., Yakopcic, C., Nasrin, M.S., Taha, T.M., Asari, V.K., 2019. Breast cancer classification from histopathological images with inception recurrent residual convolutional neural network. *Journal of digital imaging* 32, 605–617.
- AlQuraishi, M., Sorger, P.K., 2021. Differentiable biology: using deep learning for biophysics-based and data-driven modeling of molecular mechanisms. *Nature Methods* 18, 1169–1180.
- Bera, A., Bhattacharjee, D., Krejcar, O., 2024a. PND-Net: plant nutrition deficiency and disease classification using graph convolutional network. *Scientific Reports* 14, 15537.
- Bera, A., Bhattacharjee, D., Nasipuri, M., 2022a. Deep neural networks fused with textures for image classification, in: *International Conference on Frontiers in Computing and Systems*, Springer, pp. 103–111.
- Bera, A., Krejcar, O., Bhattacharjee, D., 2024b. RAFA-Net: Region attention network for food items and agricultural stress recognition. *IEEE Transactions on AgriFood Electronics* doi:10.1109/TAFE.2024.3466561.
- Bera, A., Nasipuri, M., Krejcar, O., Bhattacharjee, D., 2023. Fine-grained sports, yoga, and dance postures recognition: A benchmark analysis. *IEEE Transactions on Instrumentation and Measurement*.
- Bera, A., Wharton, Z., Liu, Y., Bessis, N., Behera, A., 2022b. SR-GNN: Spatial relation-aware graph neural network for fine-grained image categorization. *IEEE Transactions on Image Processing* 31, 6017–6031.
- Berenguer, A.D., Kvasnytsia, M., Bossa, M.N., Mukherjee, T., Deligiannis, N., Sahli, H., 2024. Semi-supervised medical image classification via distance correlation minimization and graph attention regularization. *Medical Image Analysis* , 103107.
- Biswas, S., Barma, S., 2024. MicrosMobiNet: A deep lightweight network with hierarchical feature fusion scheme for microscopy image analysis in mobile-edge computing. *IEEE Internet of Things Journal* 11, 8288–8298.
- Borkowski, A.A., Bui, M.M., Thomas, L.B., Wilson, C.P., DeLand, L.A., Mastorides, S.M., 2019. Lung and colon cancer histopathological image dataset (LC25000). *arXiv preprint arXiv:1912.12142* .
- Bui, D.C., Song, B., Kim, K., Kwak, J.T., 2024. DAX-Net: a dual-branch dual-task adaptive cross-weight feature fusion network for robust multi-class cancer classification in pathology images. *Computer Methods and Programs in Biomedicine* , 108112.
- Cai, X., Li, X., Razmjoooy, N., Ghadimi, N., 2021. Breast cancer diagnosis by convolutional neural network and advanced thermal exchange optimization algorithm. *Computational and Mathematical Methods in Medicine* 2021, 5595180.
- Cao, L., Pan, K., Ren, Y., Lu, R., Zhang, J., 2024. Multi-branch spectral channel attention network for breast cancer histopathology image classification. *Electronics* 13, 459.
- Chen, X., Zhou, J., Ke, P., Huang, J., Xiong, D., Huang, Y., Ma, G., Ning, Y., Wu, F., Wu, K., 2023. Classification of schizophrenia patients using a graph convolutional network: A combined functional mri and connectomics analysis. *Biomed. Signal Process. and Control* 80, 104293.
- Chollet, F., 2017. Xception: Deep learning with depthwise separable convolutions, in: *Proc. IEEE CVPR*, pp. 1251–1258.
- Ding, S., Gao, Z., Wang, J., Lu, M., Shi, J., 2023. Fractal graph convolutional network with mlp-mixer based multi-path feature fusion for classification of histopathological images. *Exp. Sys. Appl.* 212, 118793.
- D'Souza, N.S., Wang, H., Giovannini, A., Foncubierta-Rodriguez, A., Beck, K.L., Boyko, O., Syeda-Mahmood, T.F., 2024. Fusing modalities by multiplexed graph neural networks for outcome prediction from medical data and beyond. *Med. Img. Anal.* 93, 103064.
- Fu, Z., Chen, Q., Wang, M., Huang, C., 2025. Transformer based on multi-scale local feature for colon cancer histopathological image classification. *Biomedical Signal Processing and Control* 100, 106970.
- Gong, R., Wang, L., Wang, J., Ge, B., Yu, H., Shi, J., 2022. Self-distilled supervised contrastive learning for diagnosis of breast cancers with histopathological images. *Comput. Bio. Med.* 146 (105641).
- Guo, D., Lin, Y., Ji, K., Han, L., Liao, Y., Shen, Z., Feng, J., Tang, M., 2024. Classify breast cancer pathological tissue images using multi-scale bar convolution pooling structure with patch attention. *Biomedical Signal Processing and Control* 96, 106607.
- Han, M., Zhao, S., Yin, H., Hu, G., Ghadimi, N., 2024. Timely detection of skin cancer: An ai-based approach on the basis of the integration of echo state network and adapted seasons optimization algorithm. *Biomedical Signal Processing and Control* 94, 106324.
- Han, Z., Wei, B., Zheng, Y., Yin, Y., Li, K., Li, S., 2017. Breast cancer multi-classification from histopathological images with structured deep learning model. *Scientific Reports* 7, 4172.

Graph Convolutional Network With Channel Splitting for Cancer Classification

- Hao, S., Jia, Y., Liu, J., Wang, Z., Liu, C., Ji, Z., Ganchev, I., 2024. ST-Double-Net: A two-stage breast tumor classification model based on swin transformer and weakly supervised target localization. *IEEE Access* 12, 117921–117933.
- He, K., Zhang, X., Ren, S., Sun, J., 2016. Deep residual learning for image recognition, in: Proc. IEEE CVPR, pp. 770–778.
- Hendrycks, D., Gimpel, K., 2016. Gaussian Error Linear Units (GELUs). arXiv preprint arXiv:1606.08415 .
- Huang, S.K., Yu, Y.T., Huang, C.R., Cheng, H.C., 2023. Cross-scale fusion transformer for histopathological image classification. *IEEE Journal of Biomedical and Health Informatics* .
- Jabeen, K., Khan, M.A., Alhaisoni, M., Tariq, U., Zhang, Y.D., Hamza, A., Mickus, A., Damaševičius, R., 2022. Breast cancer classification from ultrasound images using probability-based optimal deep learning feature fusion. *Sensors* 22, 807.
- Jabeen, K., Khan, M.A., Damaševičius, R., Alsenan, S., Baili, J., Zhang, Y.D., Verma, A., 2024a. An intelligent healthcare framework for breast cancer diagnosis based on the information fusion of novel deep learning architectures and improved optimization algorithm. *Engineering Applications of Artificial Intelligence* 137, 109152.
- Jabeen, K., Khan, M.A., Hameed, M.A., Alqahtani, O., Alouane, M., Masood, A., 2024b. A novel fusion framework of deep bottleneck residual convolutional neural network for breast cancer classification from mammogram images. *Frontiers in Oncology* 14, 1347856.
- Jiang, Y., Chen, L., Zhang, H., Xiao, X., 2019. Breast cancer histopathological image classification using convolutional neural networks with small SE-ResNet module. *PLoS One* 14, e0214587.
- Joseph, A.A., Abdulla, M., Junaidi, S.B., Ibrahim, H.H., Chiroma, H., 2022. Improved multi-classification of breast cancer histopathological images using handcrafted features and deep neural network (dense layer). *Intelligent Systems with Applications* 14, 200066.
- Kassani, S.H., Kassani, P.H., Wesolowski, M.J., Schneider, K.A., Deters, R., 2019. Classification of histopathological biopsy images using ensemble of deep learning networks, in: Proc. 29th Annual Intl. Conf. on Computer Science and Software Engineering, pp. 92–99.
- Kipf, T.N., Welling, M., 2017. Semi-supervised classification with graph convolutional networks, in: Intl. Conf. Learn. Representations.
- Kulandaivelu, G., Taluja, A., Gawas, M., Nath, R.K., 2024. Automated breast cancer diagnosis optimized with higher-order attribute-enhancing heterogeneous graph neural networks using mammogram images. *Biomedical Signal Processing and Control* 97, 106659.
- Li, G., Wu, G., Xu, G., Li, C., Zhu, Z., Ye, Y., Zhang, H., 2023a. Pathological image classification via embedded fusion mutual learning. *Biomedical Signal Processing and Control* 79, 104181.
- Li, J., Zhang, J., Sun, Q., Zhang, H., Dong, J., Che, C., Zhang, Q., 2020. Breast cancer histopathological image classification based on deep second-order pooling network, in: 2020 International Joint Conference on Neural Networks (IJCNN), IEEE, pp. 1–7.
- Li, L., Mei, Z., Li, Y., Yu, Y., Liu, M., 2024a. A dual data stream hybrid neural network for classifying pathological images of lung adenocarcinoma. *Computers in Biology and Medicine* 175, 108519.
- Li, W., Long, H., Zhan, X., Wu, Y., 2024b. MDAA: multi-scale and dual-adaptive attention network for breast cancer classification. *Signal, Image and Video Processing* , 1–11.
- Li, Y., Daho, M.E.H., Conze, P.H., Zeghlache, R., Le Boit  , H., Tadayoni, R., Cochener, B., Lamard, M., Quellec, G., 2024c. A review of deep learning-based information fusion techniques for multimodal medical image classification. *Computers in Biology and Medicine* , 108635.
- Li, Y., Xie, S., Wan, Z., Lv, H., Song, H., Lv, Z., 2023b. Graph-powered learning methods in the internet of things: A survey. *Machine Learning with Applications* 11, 100441.
- Lin, J., Han, G., Pan, X., Liu, Z., Chen, H., Li, D., Jia, X., Shi, Z., Wang, Z., Cui, Y., et al., 2022. PDBL: Improving histopathological tissue classification with plug-and-play pyramidal deep-broad learning. *IEEE Trans. Medical Imaging* 41, 2252–2262.
- Liu, H., Ghadimi, N., 2024. Hybrid convolutional neural network and flexible dwarf mongoose optimization algorithm for strong kidney stone diagnosis. *Biomedical Signal Processing and Control* 91, 106024.
- Liu, L., Wang, Y., Zhang, P., Qiao, H., Sun, T., Zhang, H., Xu, X., Shang, H., 2024a. Collaborative transfer network for multi-classification of breast cancer histopathological images. *IEEE Journal of Biomedical and Health Informatics* 28, 110–121.
- Liu, Y., Zhu, Y., Gu, Z., Pan, J., Li, J., Fan, M., Li, L., Zeng, T., 2024b. Enhanced dual contrast representation learning with cell separation and merging for breast cancer diagnosis. *Computer Vision and Image Understanding* 247, 104065.
- Van der Maaten, L., Hinton, G., 2008. Visualizing Data using t-SNE. *Journal of Machine Learning Research* 9.
- Maurya, R., Pandey, N.N., Dutta, M.K., Karnati, M., 2024. FCCS-Net: Breast cancer classification using multi-level fully convolutional-channel and spatial attention-based transfer learning approach. *Biomedical Signal Processing and Control* 94, 106258.
- Maurya, R., Pathak, V.K., Dutta, M.K., 2021. Deep learning based microscopic cell images classification framework using multi-level ensemble. *Comput. Meth. Programs in Biomedicine* 211, 106445.
- Mehta, S., Lu, X., Wu, W., Weaver, D., Hajishirzi, H., Elmore, J.G., Shapiro, L.G., 2022. End-to-End diagnosis of breast biopsy images with transformers. *Medical Image Analysis* 79, 102466.
- Mudeng, V., Farid, M.N., Ayana, G., Choe, S.w., 2023. Domain and histopathology adaptations-based classification for malignancy grading system. *The American J. Path.* 193, 2080–2098.
- Niyas, S., Bygari, R., Naik, R., Viswanath, B., Ugwekar, D., Mathew, T., Kavya, J., Kini, J.R., Rajan, J., 2023. Automated molecular subtyping of breast carcinoma using deep learning techniques. *IEEE J. Translational Engg. in Health and Medicine* 11, 161–169.
- Noaman, N.F., Kanber, B.M., Smadi, A.A., Jiao, L., Alsmadi, M.K., 2024. Advancing oncology diagnostics: AI-Enabled early detection of lung cancer through hybrid histological image analysis. *IEEE Access* 12, 64396–64415.
- Oei, R.W., Hou, G., Liu, F., Zhong, J., Zhang, J., An, Z., Xu, L., Yang, Y., 2019. Convolutional neural network for cell classification using microscope images of intracellular actin networks. *PLoS one* 14, e0213626.
- Pan, X.L., Hua, B., Tong, K., Li, X., Luo, J.L., Yang, H., Ding, J.R., 2025. EL-CNN: An enhanced lightweight classification method for colorectal cancer histopathological images. *Biomedical Signal Processing and Control* 100, 106933.
- Peng, J., Peng, L., Zhou, Z., Han, X., Xu, H., Lu, L., Lv, W., 2024. Multi-level fusion graph neural network: Application to PET and CT imaging for risk stratification of head and neck cancer. *Biomedical Signal Processing and Control* 92, 106137.
- Ramirez-Bautista, J.A., Chaparro-C  denas, S.L., Esmer, C., Huerta-Ruelas, J.A., 2024. Artificial intelligence approaches to physiological parameter analysis in the monitoring and treatment of non-communicable diseases: A review. *Biomedical Signal Processing and Control* 87, 105463.
- Razmjoo, N., Ramezani, M., Ghadimi, N., 2017. Imperialist competitive algorithm-based optimization of neuro-fuzzy system parameters for automatic red-eye removal. *International Journal of Fuzzy Systems* 19, 1144–1156.
- Razmjoo, N., Sheykhhahmad, F.R., Ghadimi, N., 2018. A hybrid neural network-world cup optimization algorithm for melanoma detection. *Open Medicine* 13, 9–16.
- Saini, M., Susan, S., 2023. VGGIN-Net: Deep transfer network for imbalanced breast cancer dataset. *IEEE/ACM Trans. Computational Biology and Bioinformatics* 20, 752–762.
- Selvaraju, R.R., Cogswell, M., Das, A., Vedantam, R., Parikh, D., Batra, D., 2017. Grad-CAM: Visual explanations from deep networks via gradient-based localization, in: Proc. IEEE international conference on computer vision, pp. 618–626.
- Sepahvand, M., Abdali-Mohammadi, F., 2023. Joint learning method with teacher-student knowledge distillation for on-device breast cancer image classification. *Comput. Bio. and Med.* 155, 106476.
- Song, Y., Zou, J., Choi, K.S., Lei, B., Qin, J., 2024. Cell classification with worse-case boosting for intelligent cervical cancer screening. *Medical Image Analysis* 91, 103014.

- Spanhol, F.A., Oliveira, L.S., Petitjean, C., Heutte, L., 2016. A dataset for breast cancer histopathological image classification. *IEEE Trans. Biomedical Engineering* 63, 1455–1462.
- Springenberg, M., Frommholz, A., Wenzel, M., Weicken, E., Ma, J., Strodthoff, N., 2023. From modern CNNs to vision transformers: Assessing the performance, robustness, and classification strategies of deep learning models in histopathology. *Med. Img. Anal.* 87, 102809.
- Srivastava, G., Chauhan, A., Pradhan, N., 2023. CJT-DEO: Condorcet's jury theorem and differential evolution optimization based ensemble of deep neural networks for pulmonary and colorectal cancer classification. *Applied Soft Computing* 132, 109872.
- Taheri, S., Golrizkhatai, Z., Basabbrain, A.A., Hazzazi, M.S., 2024. A comprehensive study on classification of breast cancer histopathological images: Binary versus multi-category and magnification-specific versus magnification-independent. *IEEE Access*.
- Talib, L.F., Amin, J., Sharif, M., Raza, M., 2024. Transformer-based semantic segmentation and cnn network for detection of histopathological lung cancer. *Biomedical Signal Processing and Control* 92, 106106.
- Toğaçar, M., Özkurt, K.B., Ergen, B., Cömert, Z., 2020. BreastNet: A novel convolutional neural network model through histopathological images for the diagnosis of breast cancer. *Physica A: Statistical Mechanics and its Applications* 545, 123592.
- Tomassini, S., Falcionelli, N., Bruschi, G., Sbrollini, A., Marini, N., Sernani, P., Morettini, M., Müller, H., Dragoni, A.F., Burattini, L., 2023. On-cloud decision-support system for non-small cell lung cancer histology characterization from thorax computed tomography scans. *Computerized Medical Imaging and Graphics* 110, 102310.
- Truong, A.M., Philips, W., Veelaert, P., 2024. Exploiting spatial attention mechanism for improved depth completion and feature fusion in novel view synthesis. *IEEE Open Journal of Signal Processing* 5, 204–212.
- Tummala, S., Kim, J., Kadry, S., 2022. BreaST-Net: Multi-class classification of breast cancer from histopathological images using ensemble of swin transformers. *Mathematics* 10, 4109.
- Uddin, A.H., Chen, Y.L., Akter, M.R., Ku, C.S., Yang, J., Por, L.Y., 2024. Colon and lung cancer classification from multi-modal images using resilient and efficient neural network architectures. *Heliyon* 10.
- Wang, C., Gong, W., Cheng, J., Qian, Y., 2022. DBLCNN: Dependency-based lightweight convolutional neural network for multi-classification of breast histopathology images. *Biomedical Signal Processing and Control* 73, 103451.
- Xiao, M., Li, Y., Yan, X., Gao, M., Wang, W., 2024. Convolutional neural network classification of cancer cytopathology images: taking breast cancer as an example, in: Proceedings of the 2024 7th International Conference on Machine Vision and Applications, pp. 145–149.
- Xu, Z., Sheykhamad, F.R., Ghadimi, N., Razmjoo, N., 2020. Computer-aided diagnosis of skin cancer based on soft computing techniques. *Open Medicine* 15, 860–871.
- Yuan, H., Kido, T., Hirata, M., Ueno, K., Imai, Y., Chen, K., Ren, W., Yang, L., Chen, K., Qu, L., et al., 2024. New vision of HookEfficientNet deep neural network: intelligent histopathological recognition system of non-small cell lung cancer. *Computers in Biology and Medicine*, 108710.
- Zeng, Y., Xu, X., 2023. Label diffusion graph learning network for semi-supervised breast histological image recognition. *Biomedical Signal Processing and Control* 80, 104306.
- Zhang, L., Zhang, J., Gao, W., Bai, F., Li, N., Ghadimi, N., 2024a. A deep learning outline aimed at prompt skin cancer detection utilizing gated recurrent unit networks and improved orca predation algorithm. *Biomedical Signal Processing and Control* 90, 105858.
- Zhang, Y., Li, Z., Han, X., Ding, S., Li, J., Wang, J., Ying, S., Shi, J., 2024b. Pseudo-data based self-supervised federated learning for classification of histopathological images. *IEEE Trans. Medical Imaging* 43, 902–915.
- Zhao, X., Bai, J.W., Guo, Q., Ren, K., Zhang, G.J., 2023. Clinical applications of deep learning in breast mri. *Biochimica et Biophysica Acta (BBA)-Reviews on Cancer* 1878, 188864.
- Zhou, Y., Zhang, C., Gao, S., 2022. Breast cancer classification from histopathological images using resolution adaptive network. *IEEE Access* 10, 35977–35991.
- Zou, Y., Chen, S., Che, C., Zhang, J., Zhang, Q., 2022. Breast cancer histopathology image classification based on dual-stream high-order network. *Biomedical Signal Processing and Control* 78, 104007.